Structural Properties and Reduction Behavior of Novel Nanostructured Pd/Gadolinia–Doped Ceria Catalysts with Tubular Morphology

6 AUTHORS, INCLUDING:

Fernando Francisco Muñoz
National Scientific and Technical Research C…
7 PUBLICATIONS **35** CITATIONS

SEE PROFILE

Leandro Acuña
National Scientific and Technical Research C…
19 PUBLICATIONS **82** CITATIONS

SEE PROFILE

R. T. Baker
University of St Andrews
76 PUBLICATIONS **1,514** CITATIONS

SEE PROFILE

Rodolfo O. Fuentes
Comisión Nacional de Energia Atómica
45 PUBLICATIONS **454** CITATIONS

SEE PROFILE

ARTICLE

Structural Properties and Reduction Behavior of Novel Nanostructured Pd/Gadolinia-Doped Ceria Catalysts with Tubular Morphology

Fernando F. Muñoz,[†] Marcelo D. Cabezas,[†] Leandro M. Acuña,[†] A. Gabriela Leyva,[‡] Richard T. Baker,[§] and Rodolfo O. Fuentes*,[†]

[†]CINSO (Centro de Investigaciones en Sólidos), CONICET-CITEDEF, J.B. de La Salle 4397, (1603) Villa Martelli, Buenos Aires, Argentina

[‡]Departamento de Física, Centro Atómico Constituyentes, CNEA, Av. Gral. Paz 1499, (1650) San Martín, Buenos Aires, Argentina

[§]EaStChem, School of Chemistry, University of St. Andrews, North Haugh, St. Andrews, Fife, KY16 9ST, United Kingdom

ABSTRACT: In this work, nanostructured 1 wt % Pd/Gd$_2$O$_3$−CeO$_2$ (Pd/GDC) mixed oxide tubes with 90 mol % CeO$_2$ were synthesized following a very simple, high yield procedure, and their properties were characterized by synchrotron radiation XRD, by X-ray absorption near-edge spectroscopy (XANES), and by scanning and high resolution electron microscopy (SEM and HRTEM). In situ XANES experiments were carried out under reducing conditions to investigate the reduction behavior of these novel tubular materials. The nanostructured mixed oxide tubes were found to have a cubic crystal phase (*Fm3m* space group) and large specific surface area (∼83 m^2 g^{-1}). The tube walls were composed of nanoparticles with an average crystallite size

of about 8 nm. The SEM and HRTEM results showed that individual tubes were composed of a curved sheet of these nanoparticles. Elemental analysis showed that Ce/Gd/Pd ratios appeared to be constant across space, suggesting compositional homogeneity in the samples. XANES results indicated that the extent of reduction of these materials was small. Nevertheless, the Ce^{3+} state was detected. These results suggest that Pd cations, most likely Pd^{2+}, formed a Pd−Ce−Gd oxide solid solution and that the Pd^{2+} was stabilized against reduction in this phase. However, incorporation of the Pd (1 wt %) into the crystal lattice of the nanostructured tubes also appeared to destabilize Ce^{4+}, favoring reduction to Ce^{3+} and giving rise to a significant increase in the reducibility of this material. Preliminary catalytic studies over Pd/GDC samples exhibited an improved catalytic activity toward CH$_4$ oxidation compared to pure GDC (either nanotubes or nanopowders).
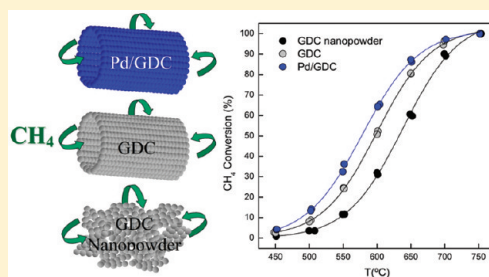
■ INTRODUCTION

Materials based on ceria are widely used for a variety of catalytic applications such as three-way catalysts,[1] solid oxide fuel cells,[2,3] and supports for the water-gas-shift reaction.[4,5] Many of these applications rely on the high oxygen ion conductivity and oxygen storage capacity that can easily be achieved in ceria by doping with other aliovalent cations, such as rare earth elements (e.g., Gd, Pr, Sm). This creates oxygen vacancies that enable migration of oxygen ions through the lattice.[6] Among these materials, one of the most promising is gadolinia-doped ceria (GDC). The defect reactions for partial substitution of Ce by Gd in GDC can be written in Kroeger−Vink notation as

$$Gd_2O_3 \xrightarrow{2CeO_2} 2Gd'_{Ce} + 3O_0^x + V_0^{\bullet\bullet} \tag{1}$$
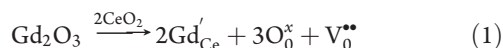
where the oxygen ion vacancies ($V_0^{\bullet\bullet}$) are responsible for the ionic conductivity of the doped ceria.[7,8] Because they exhibit high ionic conductivity at moderate temperatures (above 600 °C), these materials are considered promising for application in electrolytes for intermediate temperature solid oxide fuel cells (IT-SOFCs). However, oxygen ion vacancies can also be created by interaction

of the ceria with the gas phase. Reducing the oxide activity in the material would create both electronic (Ce'_{Ce}) and ionic ($V_0^{\bullet\bullet}$) charge carriers through the loss of molecular oxygen, according to eq 2.

$$2Ce_{Ce}^x + O_0^x \xrightarrow{2CeO_2} \frac{1}{2}O_2 + 2Ce'_{Ce} + V_0^{\bullet\bullet} \tag{2}$$
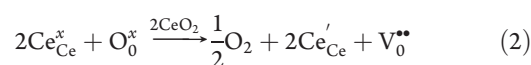
The presence of both ionic and electronic charge carriers gives rise to mixed (ionic and electronic) conducting behavior in GDC in reducing atmospheres. This is a difficulty for the application of GDC in SOFC electrolytes, where electronic conductivity would give rise to an internal short circuit of the electrolyte, but would be an advantage for the use of GDC in anodes for IT-SOFCs. Several studies in this area have been reported, especially on the use of GDC as a catalyst support.[9−12] For this application, in particular, it is necessary to obtain materials with large specific surface area (SSA) and high porosity.

The wide use of these systems as catalyst components has prompted a renewed interest in the preparation of these materials in the form of nanosized, high surface area powders. In this context, we recently reported the preparation of nanotubes of Ce-based mixed oxides, which are attractive for several reasons.[13,14] First, nanotubes with sufficiently small dimensions would have high specific surface areas (SSAs) that would lead to high activities, good atomic efficiencies, and rapid response to changing conditions in catalyst systems. Second, the tubular nanostructure, in itself, may confer additional advantages such as higher thermal, chemical, and structural stability. In our previous work and in the present contribution, the template synthesis method was employed to prepare mixed oxide nanotubes.[15−17] The preparation of nanotube structures has been suggested as a way for improving catalytic behavior. Recently, Gonzalez-Rovira et al. reported the synthesis of CeO_2 nanotubes.[18] The catalytic activity of these novel materials for the CO oxidation reaction was compared to that of a polycrystalline CeO_2 powder sample prepared by a conventional route. The activity of the CeO_2 nanotubes was shown to be of the order of 400 times higher per gram of oxide at 200 °C. In another recent study, nanotubes of $CeO_2-Gd_2O_3$ mixed oxides were reported to exhibit oxygen storage capacity (OSC) values higher than those of the conventional GDC mixed oxide.[19]

A further advantage of nanostructured ceria materials is that they can be used as supports for highly dispersed noble metal nanoparticles. The resulting catalyst systems exhibit much improved catalytic activity and redox properties. The most widely used material for this purpose is CeO_2-ZrO_2 because these compositions can undergo fast and reversible redox reactions. Several investigators have reported on the noble metal−ceria interaction and its effects on catalytic activities. In particular, Pd-based catalysts are active for NO reduction and CO and hydrocarbon oxidation reactions. The presence of Pd in the lattice of ceria-based catalysts for methane combustion has been reported to show a beneficial catalytic effect.[20] Substitution of Pd^{2+} ions for Ce^{4+} in nano-CeO_2 particles can lead to the highest possible dispersion for a given loading of Pd and to higher chemical and structural stability of the Pd^{2+} ions because of the stabilizing effect of the oxygen ions in the CeO_2 lattice.[21]

Priolkar et al. reported that Pd/CeO_2 (1 at. %) prepared by the solution-combustion method formed a solid solution, $Ce_{1-x}Pd_xO_{2-y}$ (0 < x < 0.03), and that the structure was refined for the composition $Ce_{0.99}Pd_{0.01}O_{1.90}$ in the fluorite structure with a 5% oxide ion vacancy concentration. This solid solution showed a higher catalytic activity for CO oxidation and NO reduction than Pd metal, PdO or Pd dispersed on CeO_2 by a conventional method.[22]

Recently, Acuña et al. reported on the synthesis of 1 wt % Pd/ZrO_2-CeO_2 mixed oxide nanotubes with 90 mol % CeO_2.[23] They found Pd cations, most likely Pd^{2+}, form a Pd−Ce−Zr oxide solid solution and that the Pd^{2+} is stabilized against reduction in this phase. The incorporation of the Pd (1 wt %) into the crystal lattice of the nanotubes also appeared to destabilize Ce^{4+} against reduction to Ce^{3+} and caused a significant increase in their reducibility.

In the present work, we report, for the first time, on the preparation of Pd/$CeO_2-Gd_2O_3$ mixed oxide nanotubes using the membrane templating technique. The nanotubes were synthesized using a commercial polycarbonate membrane (with a pore size of 800 nm) as a template. To determine the effect of Pd incorporation on structural properties, the resulting

nanotubes were characterized by employing synchrotron radiation X-ray diffraction (SR-XRD), X-ray absorption near-edge spectroscopy (XANES), scanning and high resolution transmission electron microscopy (SEM and HRTEM), and energy dispersive X-ray spectroscopy (EDS). The reduction behavior of these novel nanotube materials was studied using in situ XANES experiments carried out under a 5% H_2/He atmosphere. Finally, preliminary tests of the catalytic activity for CH_4 oxidation were performed on these novel materials.

■ EXPERIMENTAL SECTION

$Ce(NO_3)_3 \cdot 6H_2O$ (99.99%, Alfa Aesar), $Gd(NO_3)_3 \cdot 6H_2O$ (99.9%, Acros), and $Pd(NO_3)_2 \cdot 2H_2O$ (Merck) were employed as precursors. Each nitrate was dissolved in pure H_2O separately and then the solutions were mixed to obtain a 1 M nitrate solution with a molar Ce/Gd/Pd stoichiometry appropriate for the preparation of 1 wt % Pd/$Gd_{0.1}Ce_{0.9}O_{1.95}$ (Pd/GDC) mixed oxide.

Templates consisting of porous polycarbonate films were used as filters in an appropriate syringe filtration system to ensure that the total volume of the pores was filled with the nitrate precursor solution. The polycarbonate (PC) films used were commercially available Isopore membrane filters from Millipore. Films with 800 nm pore pass diameters were used. The reaction to obtain the desired compound proceeded by the dehydration and denitrification of the confined precursor in a commercial microwave oven. For all compositions, an output power of 800 W was applied for 3 min. The desired compound was finally obtained, and the template was burned off in a standard furnace employing a thermal treatment in which the final step involved heating in air at 650 °C for 10 min. After this treatment, the furnace was allowed to cool freely to room temperature. The resulting material was a collection of tubular nanostructures whose diameters depended on the size of the pores of the template. For the purpose of comparison, pure $Gd_{0.1}Ce_{0.9}O_{1.95}$ (GDC) nanotubes were also prepared according to Fuentes et al.[14]

Some of the 1 wt % Pd/GDC nanotube catalyst sample was reduced in 7% H_2/N_2 (balance N_2, 20 mL min^{-1}) at 450 °C for 1 h to obtain metallic palladium particles on the nanotube catalysts. In the following, this sample will be denoted Pd/GDC-R.

Synchrotron XRD experiments were carried out using the D10B-XPD beamline of the LNLS (Brazilian Synchrotron Light Laboratory, Campinas, Brazil) in static air. A high-intensity (low-resolution) configuration, without a crystal analyzer, was employed. The wavelength was set at 1.5500(4) Å. Data in the angular region of $2\theta = 20-100°$ were collected at room temperature in a step-scanning mode, with a step length of 0.05° and a step-counting time of 3 s. NIST SRM 640c Si powder was used as the standard for the instrumental broadening correction.

SEM images were obtained using a Philips XL30 E-SEM instrument that was fitted with a field emission gun. TEM images of the nanotube sample were obtained using a JEOL 2010 TEM instrument. This was equipped with a LaB_6 filament and a Gatan digital camera and was operated at 200 keV. The microscope also benefited from a system for performing energy dispersive X-ray spectroscopy (EDS), and this was used to record elemental maps. For the TEM study, samples were prepared by dipping a 3 mm copper grid coated with holey carbon film into a dispersion of the sample powder in hexane.

In order to determine qualitatively the oxidation state of Ce in the Pd/GDC nanotube samples, XANES (X-ray absorption near-edge structure) spectra were collected at the D04B-XAFS1

beamline at LNLS in transmission mode using a Si(111) monochromator for the Ce L$_3$-edge. The nominal photon flux of the beamline is 3×10^9 photons/(s·mrad·100 mA)@6 keV. All spectra were collected at room temperature for energies in the range 5690−5780 eV using steps of 2 eV for 5690−5710 and 0.2 eV for 5710−5780 eV, with $E/\Delta E$ = 5000−10000. Energy was calibrated using a Cr foil. Several acquisitions (around four spectra) were carried out on the same sample to improve the signal-to-noise ratio.

In situ XANES experiments under conditions of controlled temperature and atmosphere were carried out using the same parameters and at the same beamline as above. Samples were diluted with boron nitride, and these mixtures were pressed into 15 mm diameter pellets (around 6 mg of sample and 70 mg of diluent were used). For the transmission measurements, the pellets were placed in a tubular quartz furnace (diameter, 20 mm; X-ray path length, 440 mm) sealed with refrigerated Kapton windows. Temperature was measured and controlled by a thermocouple passed down the sample holder and positioned close to the surface of the pellet. Temperature-resolved XANES spectra at the Ce L$_{III}$-edge were acquired during temperature programmed reduction (TPR) under 5% H$_2$/He (total flow: 20 mL·min^{-1}) at temperatures from 25 to 450 °C at a heating rate of 10 °C·min^{-1} and with a total data acquisition time of 8 min per spectrum. The data were normalized using the program WinXAS.[24]

To carry out XANES experiments at the Pd L$_{III}$-edge, measurements of soft X-rays were performed at the D04A-SXS beamline of the LNLS. The powdered samples were placed on a carbon tape. X-ray absorption spectra were recorded in total electron yield (TEY) mode, collecting the emitted current at each photon energy with an electrometer connected to the sample ($E/\Delta E$ = 5000). Experiments were performed under high vacuum (10^{-8} mbar) at room temperature. The energy scale was calibrated by setting the Pd L$_{III}$-edge, defined by the first inflection point of the X-ray absorption spectrum of a Pd metallic foil, to be 3173.4 eV.

Catalytic studies were performed in a fixed-bed flow reactor (quartz tube of 4 mm internal diameter, 60 cm length), operated isothermally at atmospheric pressure. The reactor was placed in an electric tubular oven equipped with a temperature controller. A thermocouple was placed axially into the quartz tube, directly into the sample as a way to provide an accurate temperature measurement. The sample (45 mg) was diluted with ground quartz wool to ensure an adequate contact with the reactants. The reactants were a mixture of methane (1.4 cm^3·min^{-1}) and air (38.5 cm^3·min^{-1}), with nitrogen added to the mixture to provide a total gas flow of 50 N cm^3·min^{-1}. To determine the noncatalytic combustion of CH$_4$ in the reactor (blank test), a fixed bed composed of only 400 mg of SiO$_2$ was evaluated. Measurements were performed in the 300−900 °C temperature range, at 50 °C increments. Several measurements were taken at each temperature until the system reached steady state. Gas analyses were performed using a Perkin-Elmer Clarus 500 gas chromatographer equipped with a thermal conductivity detector, an Altech CTR1 packed column, and using He as the carrier gas. Moisture was removed from the gases using a desiccant trap prior to injection into the chromatograph.

■ RESULTS AND DISCUSSION

SEM and TEM Studies. Samples of the Pd-containing GDC nanotube material after reduction in 7% H$_2$ at 450 °C (referred to as Pd/GDC-R) were examined by electron microscopy. The SEM images in Figure 1a−d, taken at increasing magnification,
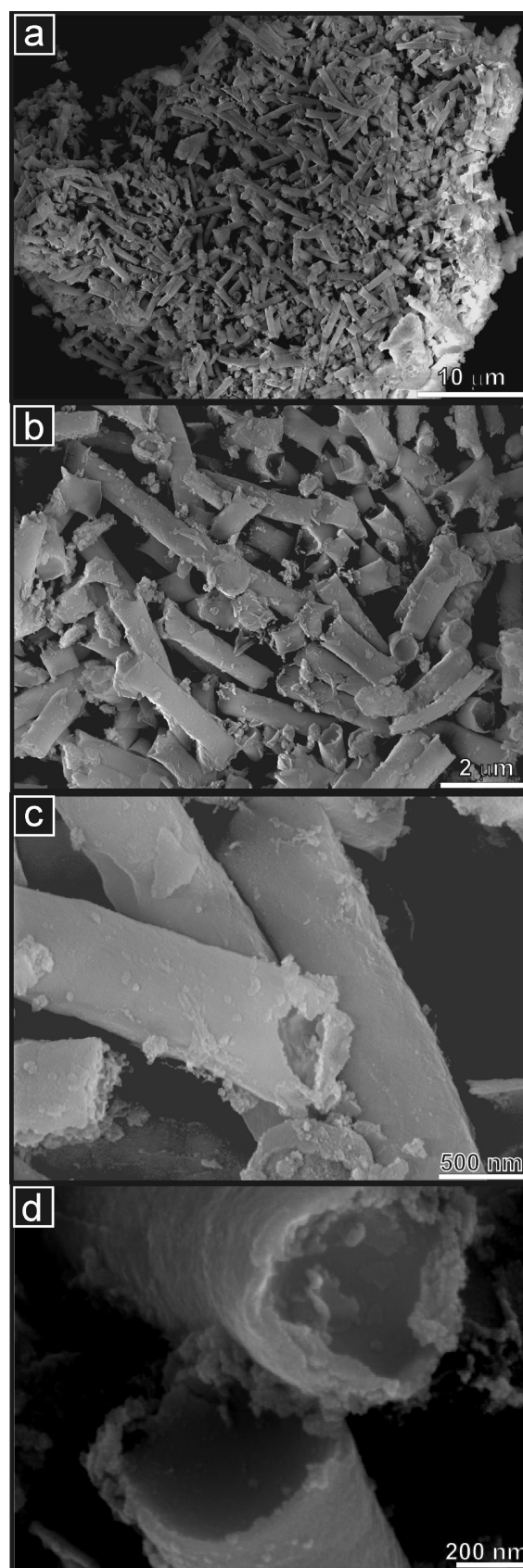
Figure 1. SEM images of the Pd/GDC nanotubes showing (a) the high yield of nanotubes; (b) the morphology of several nanotubes; and (c and d) the end of a nanotube, where the granular surface structure and the thinness of the nanotube wall are evident.
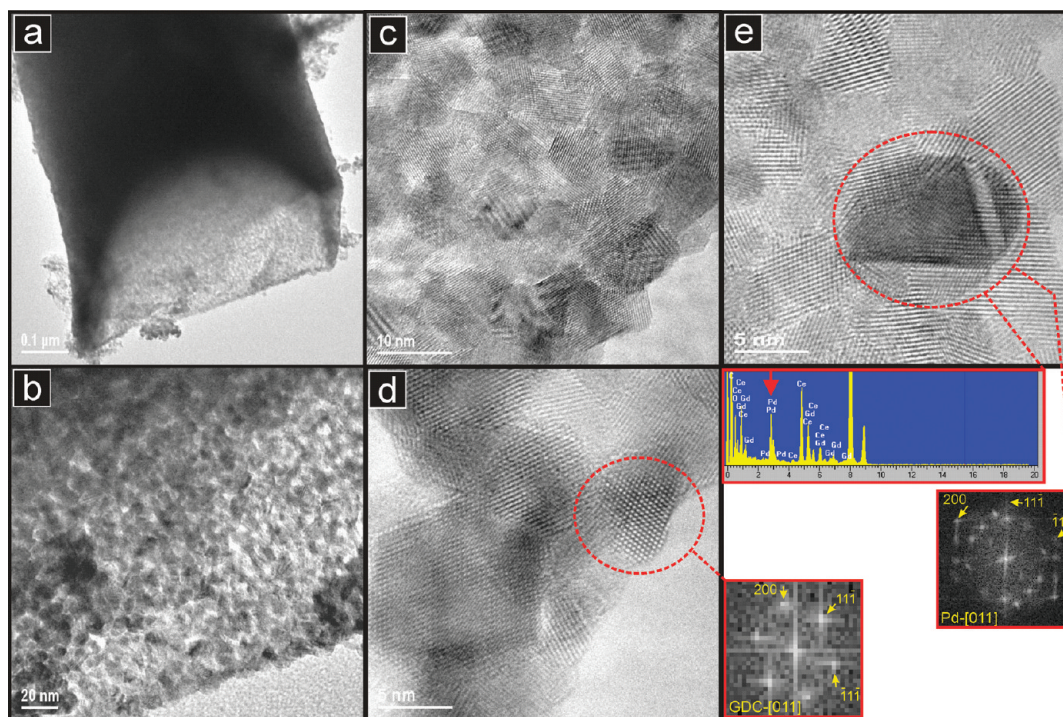
Figure 2. TEM images showing (a) the end of a nanotube at low magnification; (b) a detail of the nanotube wall; (c) the oxide nanocrystals that comprise the nanotube walls at higher magnification; (d) a high resolution image showing the crystal structure of one oxide nanocrystal (the DDP of the nanoparticle circled is also given and is indexed to the [011] zone axis of the cubic Fluorite structure of $Ce_{0.9}Gd_{0.1}O_{1.95}$); and (e) a nanoparticle of Pd (circled), as identified from the EDS spot spectrum (inset) and the DDP (inset). The DDP contains spots (indicated) that can be indexed to the [011] zone axis of the cubic Pd structure, despite some extra spots in the pattern resulting from the underlying oxide crystallites and from Moiré fringes caused by double diffraction effects.

are typical of the sample. Figure 1a and b show a large cluster of nanotubes and illustrate the very high yield of nanotubes obtained. Very little extraneous material is evident. Individual nanotubes showed consistent geometries, especially in terms of their diameters, which were typically between 500 and 600 nm. Nanotube lengths varied more than diameter, falling into the range from 1 to 5 μm. Wall thicknesses were measured from images in which nanotubes were viewed end-on, such as Figure 1d, to be around 20 nm. The granular texture observed on the nanotube surfaces at the higher magnifications suggested that the nanotube walls were composed of very small grains or nanoparticles. This was confirmed in the TEM images. The TEM images in Figure 2, in which the end of a nanotube is imaged at increasing magnifications, are typical. The nanotubes were seen to be composed, essentially, of a thin sheet of nanoparticles curved round to form the tubular structure. These nanoparticles are suggested by the contrast variations in Figure 2a but are clearly imaged at much higher magnification in Figure 2b—d. Here, individual particles are seen to have typical diameters of around 8 nm and to be crystalline. Figure 2d shows a particle (circled) whose internal crystal structure is aligned with the electron beam and can be indexed to the pseudo-Flourite structure viewed along the [011] zone axis. The corresponding digital diffraction pattern (DDP) of this particle is also given in the figure. The interplanar spacing of the (111) planes, for example, was measured to be 3.1 Å, which is consistent with a CeO_2-based oxide. Because the sample had been prereduced, it might be expected that some particles of metallic Pd would form. However, despite a prolonged study in the TEM, only one Pd

particle was identified unambiguously. The image of this particle is given in Figure 2e. The DDP of the vicinity of this particle is inset in the figure. Most of the spots in the pattern relate to crystal planes of the various underlying oxide crystallites. However, spots which are consistent with Pd viewed along the [011] zone axis were also identified and are indicated in the DDP. An EDS spectrum was also obtained by placing the focused electron beam on this particle. The spectrum is given in Figure 2 and shows a large Pd peak (arrowed). EDS spot analyses were performed routinely at many points in the sample and, in general, gave low but nonzero signals for Pd. This would suggest that Pd was distributed essentially uniformly throughout the sample. This was confirmed when elemental maps of individual nanotubes were obtained. The TEM image in Figure 3a shows two contacted nanotubes viewed side-on and a circular fragment, possibly a nanotube section viewed approximately end-on. The corresponding elemental maps of O, Ce, Gd, and Pd are presented below this image (they are slightly rotated because of the different geometries of the electron and X-ray detectors). The concentrations of these elements, including the Pd, appear to vary together across the image as a function of total sample thickness. This suggests that these elements were uniformly distributed throughout the sample mass and, therefore, that the composition of the material is at least approximately constant.

SR-XRD Studies. Synchrotron XRD patterns recorded at room temperature for the GDC and Pd/GDC nanotube samples (Figure 4) exhibited resolvable peaks but with relatively severe line broadening. This broadening was ascribable to the presence of small crystallites. The average crystallite size, D_{XRD}, was
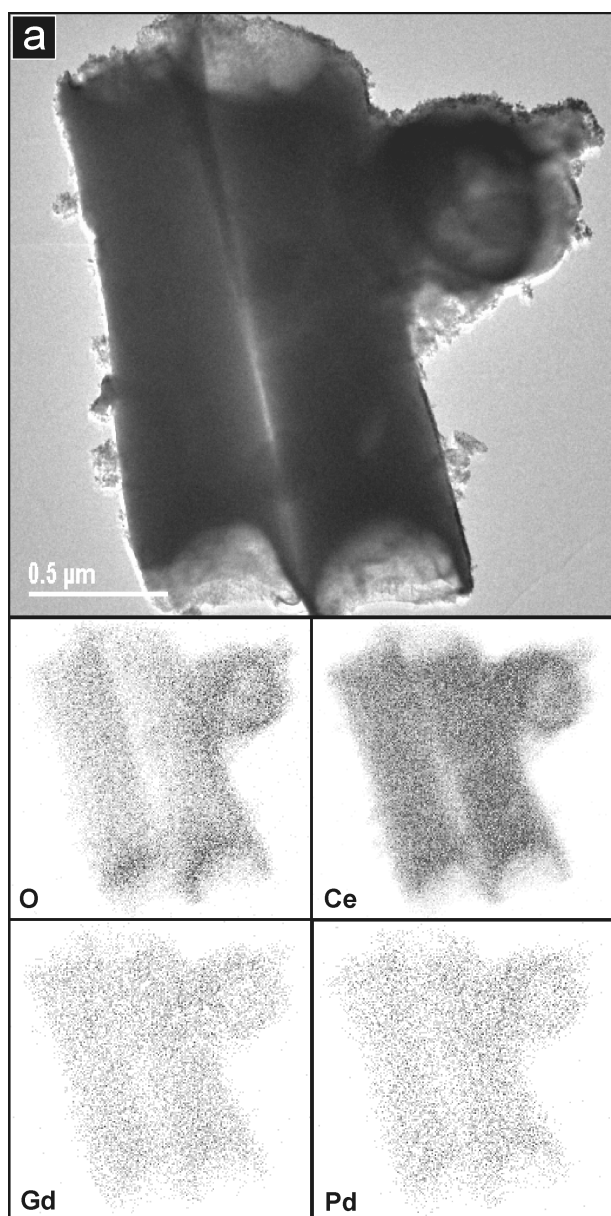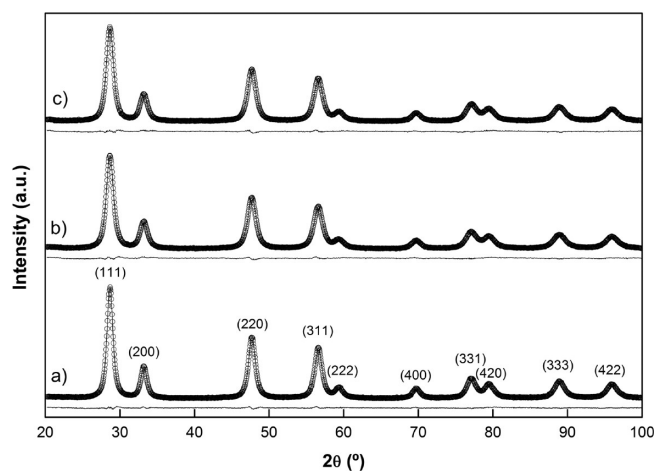
Figure 3. TEM image of a single Pd/GDC nanotube (a) with corresponding EDS maps of the elements indicated.

Figure 4. Synchrotron XRD pattern recorded at room temperature (empty circles) with the Rietveld-fitted pattern (line) and the difference plot for (a) GDC, (b) Pd/GDC, and (c) Pd/GDC-R.

determined using the Scherrer formula,[25] at the peak position of the main reflection (111). Errors in crystallite size were derived by estimating the error in the fwhm (full-width at half-maximum) to be equal to the 2θ step.[26] All samples exhibited a small average crystallite size. Samples containing Pd exhibited smaller values (7.2 ± 0.4 nm) than the pure GDC nanotubes (8.7 ± 0.4 nm). BET measurements, however, showed that the pure GDC nanotubes exhibited higher values of SSA than the Pd/GDC nanotubes (97 and 83 m$^2 \cdot$g^{-1}, respectively). No change in crystallite size was observed in the Pd/GDC samples after the reduction treatment. In these calculations, no allowance was made for possible strain in the crystal lattice. However, there was good agreement between the values obtained by this method and those obtained from the TEM study, with which they can be compared directly.

No diffraction lines corresponding to Pd or PdO were observed in the SR-XRD pattern of Pd/GDC (Figure 4b,c).

Even a slow scan in the regions of the Pd (111) and PdO (111) peaks did not show any indication of Pd metal or PdO. However, this fact is not conclusive because of the limitations of the XRD technique for detecting small amounts of minority phases.

A crystallographic study was performed by Rietveld refinement of the XRD data employing the FullProf suite of software.[27] For the cubic phase, the *Fm3m* space group was assumed, with (Gd^{3+}, Ce^{4+}) cations and O^{2-} anions in 4a and 8c positions, respectively. The peak shape was assumed to be a pseudo-Voigt function. The background of each profile was fitted using a six-parameter polynomial function in $(2\theta)^n$, $n = 0-5$. The thermal parameters were assumed to be equal. The best fits of the Pd/GDC patterns were obtained when the Pd atoms were included in the structure, with (Pd^{2+}) cation in 4a positions, and when the oxygen occupancy parameter was not fixed. The results of Rietveld refinements of the XRD data for the nanotube samples are summarized in Table I. In this table, the refinements are accompanied by reliability indices to judge the fitting quality. These indices are weighted R (R_{wp}), the reduced chi-square (χ^2), and R_e, which is related just to the profile of the XRD patterns, and R_p, which is related to the crystal structure. The reduced chi-square is defined by $(R_{wp}/R_e)^2$, where R_{wp} is the index that should be analyzed to verify if the refinement is converging and R_e is the expected statistical value for R_{wp}.[27]

No changes were observed in the lattice parameter, even when Pd was incorporated into the GDC. Because Pd^{2+} has a lower ionic radius than Ce^{4+} (0.86 vs 0.97 Å), one would expect a decrease in the lattice parameter. However, it should be noted that, for Pd^{2+}, the ionic radius value corresponds to the six-coordinated environment in PdO and the Ce^{4+} value corresponds to the eight-coordinated environment in CeO$_2$. In our case, Pd^{2+} appears to have a higher coordination number than six, because it is forced into the GDC lattice and consequently into a normally eight-coordinated environment. Undoubtedly, the oxygen vacancies that are incorporated into the GDC structure with the Pd^{2+} ions (which are mentioned in the next section) mean that the coordination number would be lower than eight but most probably higher than six. Because ionic radius increases with coordination number, the value for Pd^{2+} in this environment probably is much closer to that of Ce^{4+}.[28−30] This suggests that doping with Pd^{2+} would probably not lead to a

8748

dx.doi.org/10.1021/jp200667e |*J. Phys. Chem. C* 2011, 115, 8744–8752

Table 1. Structural Parameters and Standard Rietveld Agreement Factors for GDC and Pd/GDC Nanotubes Calcined at 650 °C for 10 Min and after Reduction (7% H$_2$, 450 °C, 1 h), Pd/GDC-R^a

| sample	GDC	Pd/GDC	Pd/GDC-R
space group	$Fm3m$	$Fm3m$	$Fm3m$
a (Å)	5.4202(6)	5.4210(9)	5.4203(8)
V (Å^3)	159.235(3)	159.311(5)	159.247(4)
Occ O	0.04064(1)	0.04003(2)	0.04011(2)
R_p	3.89	4.08	3.97
R_{wp}	3.58	3.88	3.65
R_e	2.14	2.19	2.19
χ^2	2.79	3.14	2.92

^{a} Occupation number of O (Occ O) corresponds to chemical occupation multiplied by site multiplicity normalized to the multiplicity of the general position of the space group.

decrease in lattice parameter in the first place. As mentioned above, incorporation of the Pd^{2+} ions occurs together with the generation of oxygen ion vacancies. This would be expected to affect the effective ionic radius of the Pd^{2+}, hence, providing an explanation for the almost unchanged lattice parameter observed in Pd/GDC vs pure GDC. It is well-known that lattice expansion in pure GDC is caused by doping with a bigger cation (Gd^{3+}) and the vacancies introduced along with it (due to its aliovalent nature).[31] In our case, we believe that the vacancies associated with the Pd^{2+} have the same effect and that, as a result, the lattice parameter remains essentially constant after Pd incorporation.

Because we are dealing with CeO$_2$ derived compounds, it could be inferred that the intrinsic content of Ce^{3+} (typical for such systems), with a 1.14 Å ionic radius, could account for the lattice expansion invoked to counter the lattice contraction expected on incorporation of Pd^{2+} only (i.e., without the associated oxygen ion vacancy considerations described above). However, as explained in the next section, Ce^{3+} content in our case is noticeable but low and, thus, cannot be responsible for the extent of lattice expansion required to explain these results.

XANES Studies. In Figure 5, the Ce L$_{III}$-edge XANES spectra of the GDC, Pd/GDC, and reduced Pd/GDC nanotube samples are compared with that of the CeO$_2$ reference (a microsized powder), and with cerium(III) nitrate. The Ce L$_{III}$-edge is frequently used as a "fingerprint" to characterize the electronic properties of ceria-based materials. However, the electronic transitions behind these XANES features are complex and not fully understood. In pure CeO$_2$, the Ce L$_{III}$-edge exhibits two clear peaks frequently labeled A and B. Peak A is a Ce^{4+} peak with the final state of 2p4f^{0}5d^1, which denotes that an electron is excited from the Ce 2p shell to its 5d shell, with no electron in the 4f shell. Peak B is also a Ce^{4+} peak, with the final state of 2p4f^{1}5d^{1}v, which denotes that in addition to an electron excited from the Ce 2p shell to the 5d shell, another electron is also excited from the valence band (O 2p shell) to the Ce 4f shell, leaving a hole (v) in the valence band. Some authors refer to peak C as a Ce^{3+} peak.[32] An additional small peak (D) is present at pre-edge and likely arises from transitions to the bottom of the conduction band.

In Figure 5 two main peaks (labeled A and B) separated by approximately 7 eV are observed in the CeO$_2$ spectrum. These two features were also detected for all other samples, with an intensity ratio close to that found in the CeO$_2$ sample. Comparing the size of peak C in these spectra for the nanotube materials
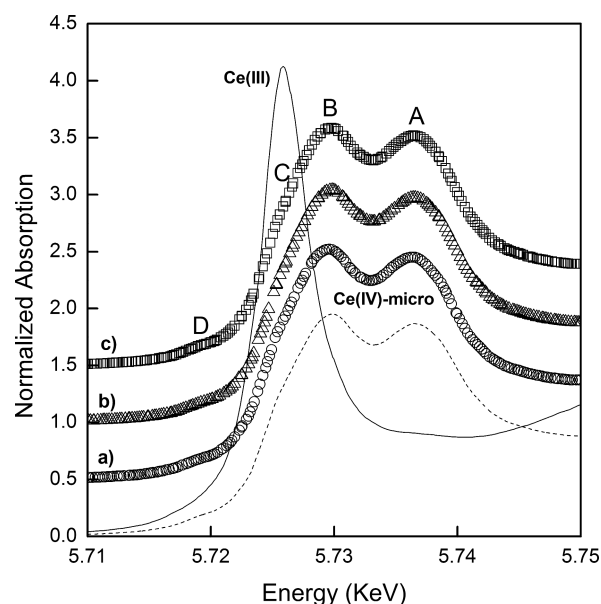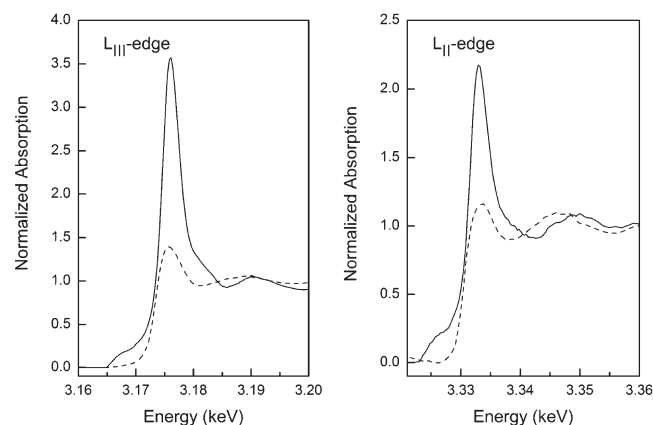

Figure 5. Ce L$_{III}$-edge XANES normalized absorption spectra for GDC (circles), Pd/GDC (triangles), and Pd/GDC-R (squares). Reference standards of microsized CeO$_2$ (dashed line), for Ce(IV), and Ce(NO$_3$)$_3$ (full line), for Ce(III), are included. Four characteristic peaks of the XANES spectra for CeO$_2$ are indicated by capital letters.

and the reference compounds, the amount of Ce^{3+} ions in the nanotube samples appears to be significant. This is attributed to an increase in the fraction of Ce ions in low coordination environments at the surface of these high surface area nanotube materials, that is, because of surface to volume effects. However, in the case of the Pd-containing samples, the Ce atoms appear to be mainly in the tetravalent state. To illustrate these differences clearly, the XANES spectrum of micro-CeO$_2$ was subtracted from each of the XANES spectra for the GDC, Pd/GDC and Pd/GDC-R nanotubes. This procedure resulted in the series of difference curves shown in Figure 6. By considering these curves in the region of peak C (compare with Figure 5), it is seen that Ce^{3+} content is higher in the pure GDC nanotubes than in the Pd-doped GDC nanotubes. This can be attributed to more pronounced surface to volume effects in the former (SSA of 97 m$^2 \cdot$g^{-1}) than in the latter (83 m$^2 \cdot$g^{-1}). Also, we propose an additional explanation for the decreased Ce^{3+} content in the Pd-doped samples: it has been reported that, in pure GDC, oxygen vacancies tend to concentrate near Gd^{3+} cations due to electrostatic effects. That is, formally positive oxygen vacancies located preferentially near the dopant cations (Gd^{3+}), which have more negative character than the host lattice cations (Ce^{4+}), thus, decreasing the fraction of Ce^{3+} ions because of an electrostatic environment that is unfavorable for them.[33−35] In Pd^{2+}-doped GDC, the oxygen ion vacancies introduced probably behave in a similar way and locate near to Pd^{2+} cations, decreasing even further the Ce^{3+} content. Basically, Pd^{2+} doping exacerbates the effect initiated by the Gd^{3+} cations, despite the lower doping level (this last fact is probably related to the greater number of vacancies introduced by the Pd cations, because one O^{2-} vacancy is associated with each Pd cation but only one vacancy for every two Gd cations).

Figure 7 shows Pd L$_{III}$-edge XANES spectra for the Pd/GDC-R samples, with the corresponding spectra of Pd metal as a reference. Clearly, a large difference is observed between the spectra of the Pd/GDC compounds and those of the Pd foil reference. A noticeable shift to higher energies is observed at
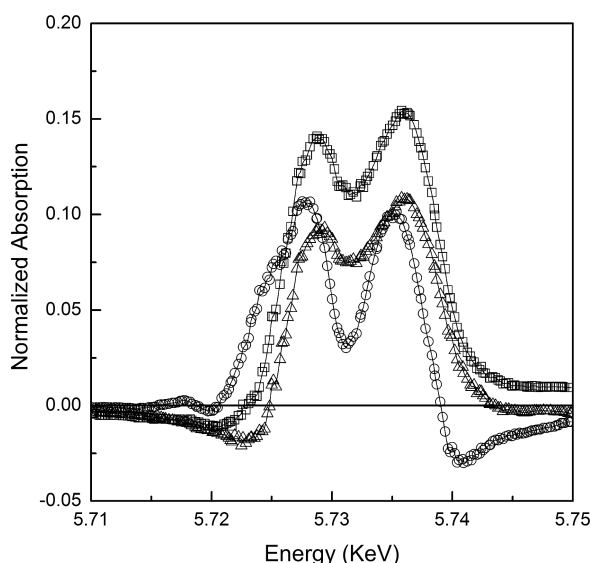
Figure 6. XANES difference spectra, obtained by subtraction of the reference spectrum of microsized CeO_2 powder (Ce^{4+}), for GDC (circles), Pd/GDC (triangles), and Pd/GDC-R (squares).

Figure 7. Normalized Pd L_{III} and L_{II}-edge XANES absorption spectra for Pd/GDC-R (full line) and Pd metal foil (dotted line) at room temperature.

both absorption edges for the Pd/GDC compounds with respect to the foil. The Pd/GDC spectra exhibit a large white line peak, which can be assigned to the electronic transition from Pd $2p_{3/2}$ to the unoccupied 4d states.[36] The L_{III}-absorption edge for Pd metal is at 3173.4 eV, while the Pd/GDC-R nanotube sample exhibited a higher value of 3174.6 eV. The reduction treatment seems not to have affected the oxidation state of the Pd in the Pd/GDC-R samples because these results indicate that the Pd was not in its metallic form and, therefore, that a solid solution of Pd and the GDC oxide was probably formed that protected the Pd from being reduced. This idea agrees well with the explanations proposed above, because these rely on the presence of Pd as the divalent cation rather than in the metallic state.

In Situ XANES Studies. To determine the fraction of Ce present as Ce^{3+} in the samples, data analysis was conducted by least-squares fitting four Gaussian profiles and one arctangent function to the experimental data in the range between 5710 and 5750 eV. The assignment of the four peaks in this region was
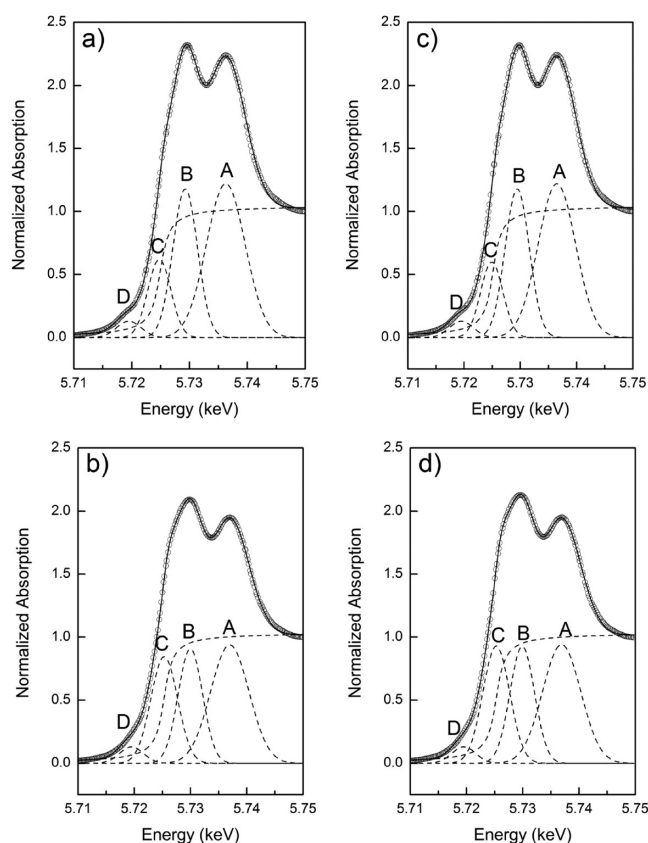

Figure 8. Normalized Ce L_{III}-edge XANES absorption spectra for (a) GDC and (c) Pd/GDC at room temperature and for (b) GDC and (d) Pd/GDC at 450 °C under reducing conditions, showing the experimental data (empty circles), four Gaussian peaks (A–D) and one arctangent function obtained by least-squares fitting (dotted lines) and the sum of all five functions (continuous line).

discussed above. In Figure 8, the Ce L_{III}-edge XANES spectra of the GDC and Pd/GDC nanotube samples under reducing conditions ($5\%H_2$/He, 20 mL·min^{-1}) at room temperature and at 450 °C and their corresponding fits are shown. In both samples, the area of peak C clearly increased and that of the white line clearly decreased on going to the higher temperature. Futhermore, at 450 °C, the area of peak C for Pd/GDC (Figure 8d) is larger than the same peak for the GDC sample (Figure 8b). This indicates that the amount of Ce present as Ce^{3+} in the Pd/GDC samples is larger than in the pure GDC nanotubes. No significant differences between Pd/GDC and Pd/GDC-R nanotubes were observed.

The ratio between the area of peak C (associated with Ce^{3+}) and the sum of the areas of peaks A, B, and C (A and B are associated with Ce^{4+}) gives direct information about the fraction of Ce present as Ce^{3+}. In Figure 9, this fraction is plotted for the different samples at different temperatures in a flow of $5\%H_2$/He. This figure clearly shows the significant increase in reducibility of these samples caused by the incorporation of Pd. It has already been proposed that the reducibility of ceria increases with Gd^{3+} doping due to the effect of the extrinsic oxygen ion vacancies on the total oxygen release/storage equilibrium (as shown in eq 2).[7,37] We can explain the further increased reducibility of the Pd/GDC sample in the same vein. That is, as a consequence of the extrinsic vacancies introduced by the Pd^{2+} cation. Because
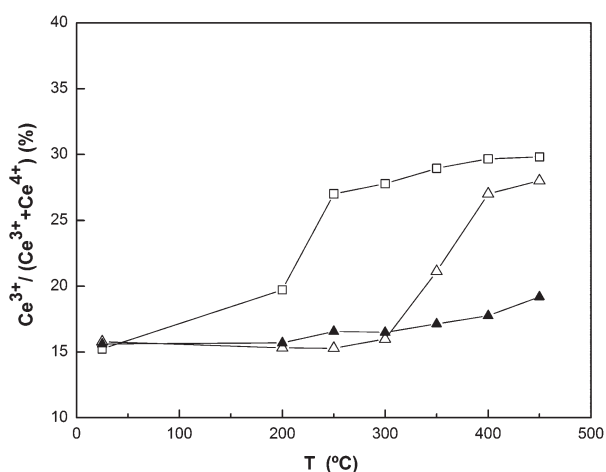
Figure 9. Fraction of Ce present as Ce^{3+} in GDC (empty triangles) and Pd/GDC (squares) nanotube samples at different temperatures under reducing conditions. GDC nanopowders (full triangles) are included for comparison.
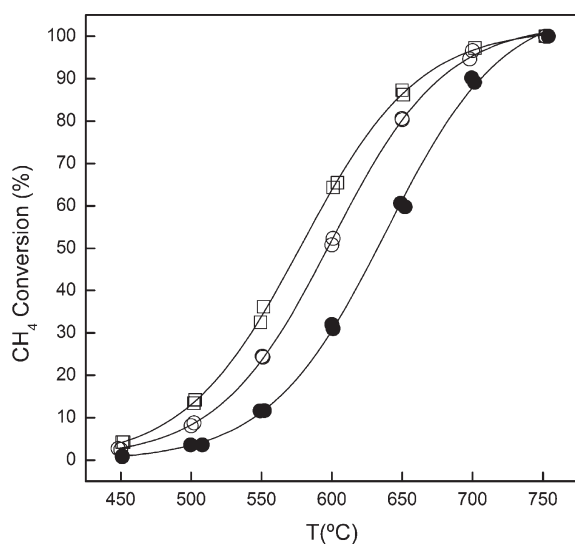
Figure 10. Catalytic results of CH_4 conversion for GDC (empty circles) and Pd/GDC (empty squares) nanotube samples at different temperatures under reducing conditions. Data for GDC nanopowders (full circles) are included for comparison.

Pd^{2+} introduces one O^{2-} vacancy per dopant cation (and Gd^{3+} introduces only one vacancy every two dopant cations), Pd^{2+} doping could be expected to show this effect, despite its low concentration. This would lead to the higher Ce^{3+} contents seen in the Pd-containing samples in Figure 9.

Preliminary Catalytic Studies. To obtain an indication of the catalytic activity and performance of the Pd/GDC system, several tests were performed as explained in the experimental section. In order to allow a comparison between samples of the same composition but different morphologies, samples of GDC nanotubes[14] and of GDC nanopowders (obtained by the citrate complexation method)[38] were also tested, thus, providing a sample with high SSA (85 $m^2 \cdot g^{-1}$) and one with a typical medium-to-low SSA (30 $m^2 \cdot g^{-1}$), respectively.

In Figure 10, CH_4 conversion versus temperature for different catalyst samples are plotted. As an index of the catalytic activity,

the half-conversion temperature (T_{50}) was used and it was estimated from experimental curves when the 50% of CH_4 conversion was reached.[39] The corresponding results show very high CH_4 conversion values for the Pd/GDC sample, which are much higher than for the other samples tested. The noncatalytic sample (blank test) exhibits the highest value of T_{50} (850 °C), and GDC nanopowders and nanotubes exhibit values of 635 and 595 °C, while the Pd/GDC sample exhibits the lowest value of T_{50} (575 °C).

The proposed explanation for this can be expressed as follows. Going from the GDC powder sample obtained using the citrate route to the undoped nanotube sample, the increase in SSA is responsible for the enhanced catalytic activity. The Pd/GDC sample benefits not only from the high SSA typical of the nanotube materials, but also exhibits an enhancement in catalytic activity attributed to the presence of the Pd^{2+}. It has already been mentioned that the Pd seemed to exist in the Pd^{2+} state in Pd/GDC and that it is uniformly distributed throughout the entire crystal lattice of the mixed oxide. Several studies have showed that these particular characteristics are strong promoters of catalytic activity for hydrocarbon conversion, thus, explaining the high CH_4 conversion values observed for this sample.[40]

■ CONCLUSIONS

In the present work, we report, for the first time, on the preparation of $Pd/CeO_2-Gd_2O_3$ mixed oxide nanotubes. The nanotubes were synthesized using a commercial polycarbonate membrane (with pore size of 800 nm) as a template. The resulting nanotubes were characterized by employing synchrotron radiation X-ray diffraction, XANES, SEM, HRTEM, and EDS. The surface area and the catalytic activity of the new material were compared to those of GDC nanotubes prepared without Pd.

Electron microscope images showed that nanotubes had been formed in very high yield. Their diameters and wall thicknesses were around 600−700 nm and about 20 nm, respectively. Nanotube lengths varied from about 1 to 5 μm. The tube walls consisted of oxide crystallites of about 8 nm diameter.

The elemental compositions of the Pd/GDC samples were verified to be homogeneous by elemental mapping of individual nanotubes. Ce, Gd, Pd, and O elements were uniformly distributed throughout the sample mass. Only a very small number of Pd particles were detected in the TEM.

In the Pd/GDC nanotubes, the presence of oxygen vacancies leads to a reduction of some Ce^{4+} to Ce^{3+}. However, the XANES results indicate that the extent of reduction of these materials is small and that the Ce^{4+} state is in the majority. XANES spectra also indicate that the Pd was not reduced in the reduction treatment used here. This and the electron microscopy results suggest that Pd cations, most likely Pd^{2+}, form a solid solution with the GDC oxide and that this stabilizes the Pd against reduction.

The addition of Pd to the nanostructured ceria-based tubes increased the reducibility of the Ce in the mixed oxide. This was demonstrated by analysis of in situ XANES spectra obtained under reducing conditions.

Preliminary catalytic studies over Pd/GDC samples exhibited an improved catalytic activity toward CH_4 oxidation compared to pure GDC (either nanotubes or nanopowders), providing an interesting avenue for future work in this area and a promising possible application for this particular system.

8751

dx.doi.org/10.1021/jp200667e |*J. Phys. Chem. C* 2011, 115, 8744–8752

AUTHOR INFORMATION

Corresponding Author
*Tel.: +541147098240. Fax: +541147098241. E-mail: rofuentes@conicet.gov.ar.

REFERENCES

(1) Di Monte, R.; Kaspar, J. *Top. Catal.* **2004**, *28*, 47–57.
(2) Park, S. D.; Vohs, J. M.; Gorte, R. J. *Nature* **2000**, *404*, 265–267.
(3) Haile, S. M. *Mater. Today* **2003**, *6*, 24–29.
(4) Kim, T.; Vohs, J. M.; Gorte, R. J. *Ind. Eng. Chem. Res.* **2006**, *45*, 5561–5565.
(5) Gorte, R. J. *AIChE J.* **2010**, *56*, 1126–1135.
(6) Kilner, J. A. *Solid State Ionics* **2000**, *123*, 13–23.
(7) Steele, B. C. H. *Solid State Ionics* **2000**, *129*, 95–110.
(8) Dalset, B.; Blennov, P.; Van Hendriksen, P.; Bonannos, N.; Lybye, D.; Mogensen, M. *J. Solid State Electrochem.* **2006**, *10*, 547–561.
(9) Primdahl, S.; Liu, Y. L. *J. Electrochem. Soc.* **2002**, *149* (11), A1466–A1472.
(10) Yaremchenko, A. A.; Valente, A. A.; Kharton, V. V.; Bashmakov, I. A.; Rocha, J.; Marques, F. M. B. *Catal. Commun.* **2003**, *4*, 477–483.
(11) Jiang, S. P.; Chen, X. J.; Chan, S. H.; Kwok, J. T. *J. Electrochem. Soc.* **2006**, *153* (5), A850–A856.
(12) Hennings, U.; Reimert, R. *Appl. Catal., B* **2007**, *70*, 498–508.
(13) Fuentes, R. O.; Acuña, L. M.; Zimicz, M. G.; Lamas, D. G.; Sacanell, J. G.; Leyva, A. G.; Baker, R. T. *Chem. Mater.* **2008**, *20* (23), 7356–7363.
(14) Fuentes, R. O.; Muñoz, F. F.; Acuña, L. M.; Leyva, A. G.; Baker, R. T. *J. Mater. Chem* **2008**, *18*, 5689–5795.
(15) Martin, C. R. *Science* **1994**, *266*, 1961–1966.
(16) Martin, C. R. *Chem. Mater.* **1996**, *8*, 1739–1746.
(17) Bae, C.; Yoo, H.; Kim, S.; Lee, K.; Kim, J.; Sung, M. M.; Shin, H. *Chem. Mater.* **2008**, *20*, 756–767.
(18) González-Rovira, L.; Sánchez-Amaya, J. M.; López-Haro, M; del Rio, E; Hungría, A. B.; Midgley, P.; Calvino, J. J.; Bernal, S.; Botana, F. J. *Nano Lett.* **2009**, *9* (4), 1395–1400.
(19) Yang, T.; Xia, D. *Mater. Chem. Phys.* **2010**, *123*, 816–820.
(20) Primavera, A.; Trovarelli, A.; de Leitenburg, C.; Dolcetti, G.; Llorca, J. *Stud. Surf. Sci. Catal.* **1998**, *119*, 87–92.
(21) Bera, P.; Patil, K. C.; Jayaram, V.; Subbanna, G. N.; Hegde, M. S. *J. Catal.* **2000**, *196*, 293–301.
(22) Priolkar, K. R.; Bera, P; Sarode, P. R.; Hegde, M. S.; Emura, S.; Kumashiro, R.; Lalla, N. P. *Chem. Mater.* **2002**, *14*, 2120–2128.
(23) Acuña, L. M.; F.F. Muñoz, F. F.; M.D. Cabezas, M. D.; D.G. Lamas, D. G.; Leyva, A. G.; Fantini, M. C. A.; Baker, R. T.; Fuentes, R. O. *J. Phys. Chem. C* **2010**, *114*, 19687–19696.
(24) Ressler, T. *J. Synchrotron Radiat.* **1998**, *5*, 118–122.
(25) Klug, H.; Alexander, L. *X-ray Diffraction Procedures for Polycrystalline and Amorphous Materials*; John Wiley: New York, 1974; p 618.
(26) Lamas, D. G.; Fuentes, R. O.; Fábregas, I. O.; Fernández de Rapp, M. E.; Lascalea, G. E.; Casanova, J. R.; Walsöe de Reca, N. E.; Craievich, A. F. *J. Appl. Crystallogr.* **2005**, *38*, 867–873.
(27) Rodríguez-Carvajal, J. *FullProf98*, Version 0.2; Laboratoire León Brillouin (CEA-CNRS): Saclay, France, 1998.
(28) Shannon, R. D.; Prewitt, C. T. *Acta Crystallogr., B* **1969**, *25*, 925–946.
(29) Shannon, R. D.; Prewitt, C. T. *Acta Crystallogr., B* **1970**, *26*, 1046–1048.
(30) Shannon, R. D. *Acta Crystallogr., A* **1976**, *32*, 751–767.
(31) Mahata, T.; Das, G.; Mishra, R. K.; Sharma, B. P. *J. Alloys Comp.* **2005**, *391*, 129–135.
(32) Zhang, F.; Wang, P.; Koberstein, J.; Khalid, S.; Chan, S.-W. *Surf. Sci.* **2004**, *563*, 74–82.
(33) Ohashi, T.; Yamazaki, S.; Tokunaga, T.; Arita, Y.; Matsui, T.; Harami, T.; Kobayashi., K. *Solid State Ionics* **1998**, *113−115*, 559–564.
(34) Borchert, H.; Borchert, Y.; Kaichev, V. V.; Prosvirin, I. P.; Alikina, G. M.; Lukashevich, A. I.; Zaikovskii, V. I.; Moroz, E. M.; Paukshtis, E. A.; Bukhtiyarov, V. I.; Sadykov, V. A. *J. Phys. Chem. B* **2005**, *109*, 20077–20086.
(35) Inaba, H.; Sagawa, R.; Hayashi, H.; Kawamura, K. *Solid State Ionics* **1999**, *122*, 95–103.
(36) Shimizu, K.; Maruyama, R.; Komai, S.; Kodama, T.; Kitayama, Y. *J. Catal.* **2004**, *227*, 202–209.
(37) Mogensen, M.; Sammes, N. M.; Tompsett, G. A. *Solid State Ionics* **2000**, *129*, 63–94.
(38) Fuentes, R. O.; Baker, R. T. *J. Power Sources* **2009**, *186*, 268–277.
(39) Specchia, S.; Conti, F.; Specchia, V. *Ind. Eng. Chem. Res.* **2010**, *49*, 11101–11111.
(40) Primet, M.; Garbowski, E. In *Catalysis by Ceria and Related Materials*; Trovarelli, A., Ed.; Imperial College Press: London, 2002; Ch. 13.

8752

dx.doi.org/10.1021/jp200667e |*J. Phys. Chem. C* 2011, 115, 8744–8752